IOPscience iopscience.iop.org

Home Search Collections Journals About Contact us My IOPscience

*Ab initio* investigations of the transport properties of Haeckelite nanotubes

This article has been downloaded from IOPscience. Please scroll down to see the full text article.

2008 J. Phys.: Condens. Matter 20 415207

(http://iopscience.iop.org/0953-8984/20/41/415207)

View the table of contents for this issue, or go to the journal homepage for more

Download details:
IP Address: 129.252.86.83
The article was downloaded on 29/05/2010 at 15:35

Please note that terms and conditions apply.

J. Phys.: Condens. Matter **20** (2008) 415207 (10pp) doi:10.1088/0953-8984/20/41/415207

# *Ab initio* investigations of the transport properties of Haeckelite nanotubes

**Ye-Fei Li, Bing-Rui Li[1] and Hao-Li Zhang**

State Key Laboratory of Applied Organic Chemistry (SKLAOC), College of Chemistry and Chemical Engineering, Lanzhou University, Lanzhou 730000, People's Republic of China

E-mail: bingruili@gmail.com

Received 9 May 2008, in final form 18 August 2008
Published 12 September 2008
Online at stacks.iop.org/JPhysCM/20/415207

**Abstract**

A systematic investigation of the electronic transport properties of Haeckelite nanotubes using *ab initio* calculation is presented. The Haeckelite nanotube is coupled with Haeckelite nanotubes and bulk Au electrodes, respectively. Negative differential resistance and nonlinear conduction phenomena have been observed in the simulated $I$–$V$ curves. Our results suggest that this behavior is attributable to the band mismatch between left and right electrodes, which implies that some intriguing electronic transport characteristics could be realized by using nanoscale electrodes.

(Some figures in this article are in colour only in the electronic version)

## 1. Introduction

Carbon science has been revolutionized by the discovery and synthesis of fullerenes [1, 2] and nanotubes [3], which have attracted intensive research efforts. It is known that defects affect the material properties significantly in many carbon-based materials. One well known form of defect that occurs in carbon nanotubes is the Stone–Wales (SW) reconstruction (as shown in figure 1). SW defects could close the gap in large-gap nanotubes, open the gap in small-gap nanotubes, and increase the density of states in metallic nanotubes [4]. Following the previous idea of improving the metallic behavior of the nanotubes, a new family of layered allotropic carbon forms, named Haeckelite, has been predicted [5]. The Haeckelite type of graphene consists of equal numbers of pentagons and heptagons in addition to any number of hexagons. Theoretical simulation reveals that these Haeckelite structures are more stable than $C_{60}$ and have energies of the order of 0.3–0.4 eV/atom [6] with respect to normal graphene. Interestingly, it is more energetically viable to roll up Haeckelite sheets into tubes, allowing the potential synthesis of this new class of nanotubes. The electronic structures of Haeckelite nanotubes (HNTs) show that the vast majority of HNTs reveal an intrinsic metallic behavior [5], while some of the HNTs, such as coiled, screwlike, curled or pearl-necklace-like nanotubes or others generated from conventional armchair nanotubes, turn out to be either narrow- or moderate-band-gap semiconductors [7, 8].

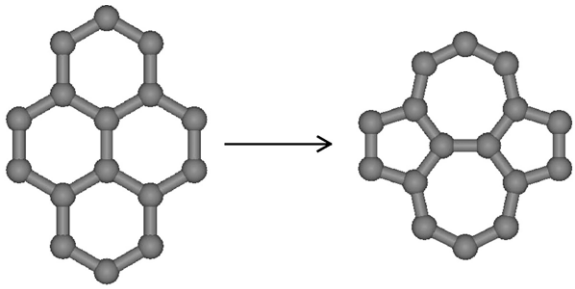

**Figure 1.** Stone–Wales reconstruction.

In this paper, the electronic transport properties of HNTs have been analyzed from the total transmission and its eigenchannel decompositions, and the characteristics of the molecular projected self-consistent Hamiltonian (MPSH) along with their band structures. It has been reported that the conducting behaviors for the capped NHTs sandwiched between metallic Ni leads are similar to armchair carbon nanotubes (CNTs) [9]. However, our results show that transport properties of HNTs are very different from that of graphitic armchair carbon nanotubes when biased via nanotube leads. What interests us is that a negative differential resistance (NDR) phenomenon has been clearly observed and tuned by the electronic structures of electrodes. In spite of a number of theoretical and experimental studies of NDR in various kinds

[1] Author to whom any correspondence should be addressed.

 © 2008 IOP Publishing Ltd Printed in the UK

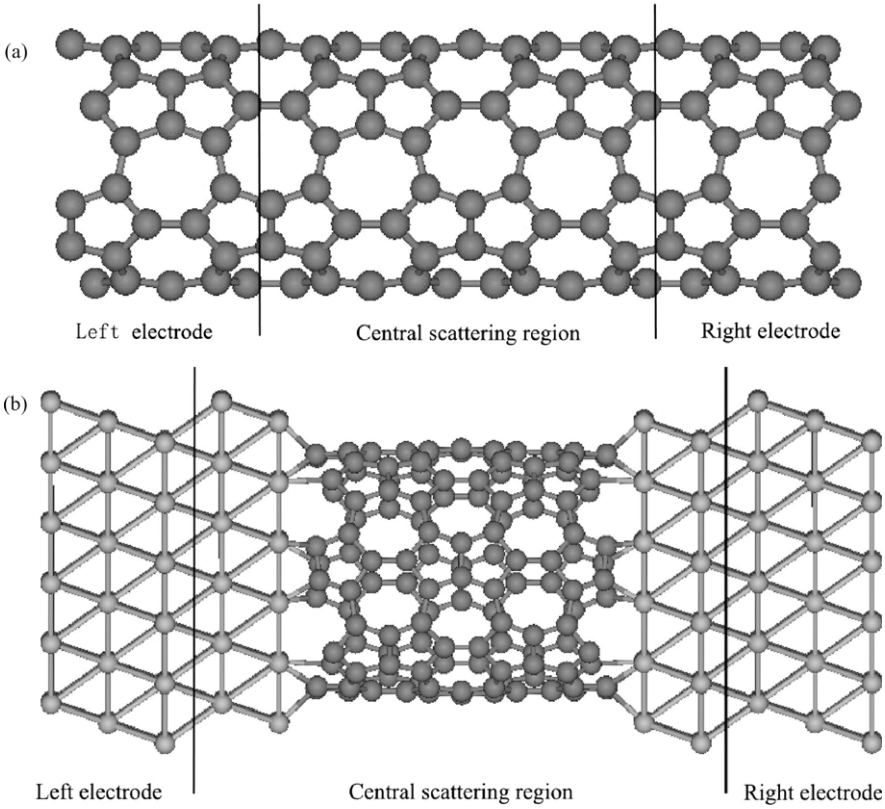


**Figure 2.** The simulation model of the HNTs coupled to (a) HNT electrodes and (b) bulk Au(111)-(6 × 6) electrodes.

of molecular devices [10–14], the origin of NDR is still under intense debate. Our calculations indicate that band mismatch between left and right electrodes is responsible for the NDR behavior of the HNT-based device.

## 2. Calculation method and simulation models

The two-probe system model has been used for the theoretical simulation (figure 2), which consists of a segment of short HNT connected with either (a) two nanoscale HNT electrodes or (b) two bulk Au(111) electrodes. The HNT could be $R_{5,7}(3, 0)$ or $R_{5,7}(4, 0)$ (the nomenclature of the HNT can be found in [5]) and only one case is shown in figure 2. The two-probe system could be divided into three parts: a scattering region and two semi-infinite electrodes. In figure 2(a), the effect of contact resistance has been avoided; while the contact resistance still exists in figure 2(b). Geometry optimization was carried out via the SIESTA program. All of the structures were fully relaxed until the maximum absolute force was less than 0.04 eV $Å^{-1}$, while the atomic positions of electrodes were fixed. It is shown by the optimized configurations (figure 2) that the HNT structure is flat when coupled to pure HNT electrodes; while it is significantly distorted when coupled to bulk Au(111) electrodes. In figure 2(b), the distances between the HNT end and the Au surface before and after relaxation are 1.6 and 1.55 Å, respectively.

The transport calculations have been performed by using the ATOMISTIX TOOLKIT (ATK) [15–18], which is based on the combination of density functional theory (DFT) with the non-equilibrium Green function (NEGF) technique. The most unique feature of ATK is the ability to calculate the electrical properties of two-probe systems.

Using the NEGF formalism [19–21] the current through the device can be derived as follows:

$$I(V) = G_0 \int_{-\infty}^{+\infty} \mathrm{d}\varepsilon \, [n_{\mathrm{F}}(\varepsilon - \mu_{\mathrm{L}}) - n_{\mathrm{F}}(\varepsilon - \mu_{\mathrm{R}})] \times \mathrm{Tr}[\mathbf{t}^{\dagger}\mathbf{t}](\varepsilon) \quad (1)$$

where $G_0 (G_0 = 2e^2/h = 77.48\ \mu\mathrm{S})$ represents the quantum of conductance, $n_{\mathrm{F}}(\varepsilon - \mu)$ is the Fermi distribution function, $\mu_{\mathrm{L}}$ and $\mu_{\mathrm{R}}$ are chemical potentials of the left and right leads, and $\mathbf{t}$ is the transmission amplitude matrix. As is known, once the bias voltage is applied, the chemical potentials $\mu_{\mathrm{L}}$ and $\mu_{\mathrm{R}}$ will be shifted correspondingly. When the temperature is not very high, such as 300 K in this calculation, equation (1) could be simplified as follows:

$$I(V) = G_0 \int_{\mu_{\mathrm{L}}}^{\mu_{\mathrm{R}}} \mathrm{d}\varepsilon \, \mathrm{Tr}[\mathbf{t}^{\dagger}\mathbf{t}](\varepsilon). \quad (2)$$

Equation (2) indicates that only the transmission in the energy region between $\mu_{\mathrm{L}}$ and $\mu_{\mathrm{R}}$ contributes to the current integral above, which is referred to as the current window.

The eigenchannels are defined in terms of the transmission amplitude matrix $\mathbf{t}$,

$$\mathbf{t} = \mathbf{U_R} \mathrm{diag}\{|\tau_n|\} \mathbf{U_R^{\dagger}} \quad (3)$$

and the total transmission can be split into individual eigenchannel contributions,

$$T = \sum_n |\tau_n|^2. \quad (4)$$

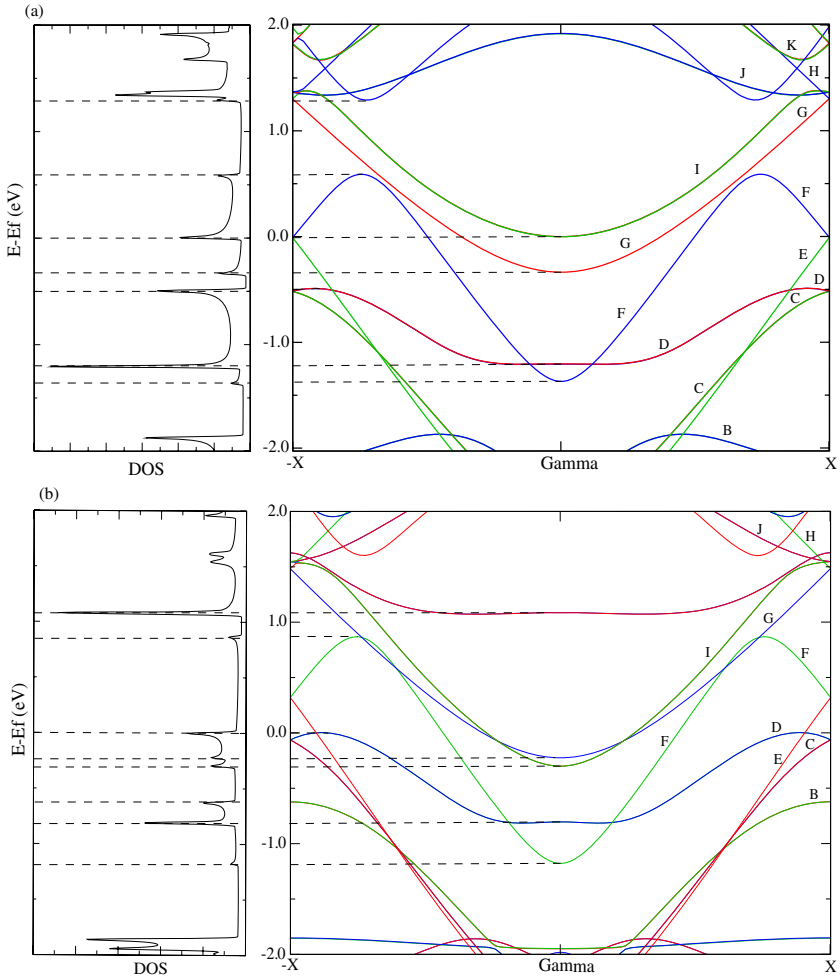


**Figure 3.** Electronic band structure and density of states in the Fermi level region of (a) $R_{5,7}(3, 0)$ and (b) $R_{5,7}(4, 0)$. Each point ($\nabla_k E = 0$) of band structure corresponds to a peak of the DOS, which is marked out with dashed lines.

The individual eigenchannel transmission gives a more detailed description of the conductance and is useful for the interpretation of the results [21–23].

In this contribution, core electrons are simulated with Troullier–Martins nonlocal norm-conserving pseudopotentials. The local density approximation with the Perdew–Zunger parametrization [24] of the correlation energy of a non-spin-polarized homogeneous electron gas calculated by Ceperley–Alder (LDA-PZ) was used to describe the exchange–correlation potential. The numerical atomic orbital basis set with a single zeta (SZ) for each valence orbital was chosen for all atoms. The convergence criterion for the density matrix and the Hamiltonian is $10^{-4}$ via the mixture of the Hamiltonian.

## 3. Results and discussion

### *3.1. Band structures and density of states of the pure HNTs*

Figure 3 shows the electronic band structure and density of states (DOS) in the Fermi level region of (a) $R_{5,7}(3, 0)$ and (b) $R_{5,7}(4, 0)$. Each band is indexed by alphabetic B, C, D etc according to the energy at the X point, and the bands B, C, D, I, J and K are doubly degenerate. It is shown that the two HNTs considered in this work exhibit a clear metallic behavior. Particularly, an unusually high intensity DOS peak at the Fermi level is noticed. This is due to the band topology of HNTs, which is characterized by several bands near the Fermi level.

The DOS is calculated as follows [25]:

$$N(E) = \frac{V}{4\pi^3} \int \frac{\mathrm{d}S}{|\nabla_k E|} \tag{5}$$

where $V$ represents the volume of the cell or supercell and $\nabla_k E$ is the energy gradient of the $k$-space. The point $\nabla_k E = 0$ of the band structure is known as the Van Hove singularity, and corresponds to a peak of the DOS, as shown in figure 3.

### *3.2. Transport properties under zero bias*

Figures 4(a) and (b), which correspond to $R_{5,7}(3, 0)$ and $R_{5,7}(4, 0)$, show the transmission spectra at zero bias for the two-probe system shown in figure 2(a). The energy is relative to the average Fermi level of the two-probe system, i.e. $(\mu_L + \mu_R)/2$. The transmission obtained with equation (4) is shown to be quantized, retrieving the conducting channels. For a molecular device of length $L$ coupled to metallic contact reservoirs, the transport through the system is ballistic if the

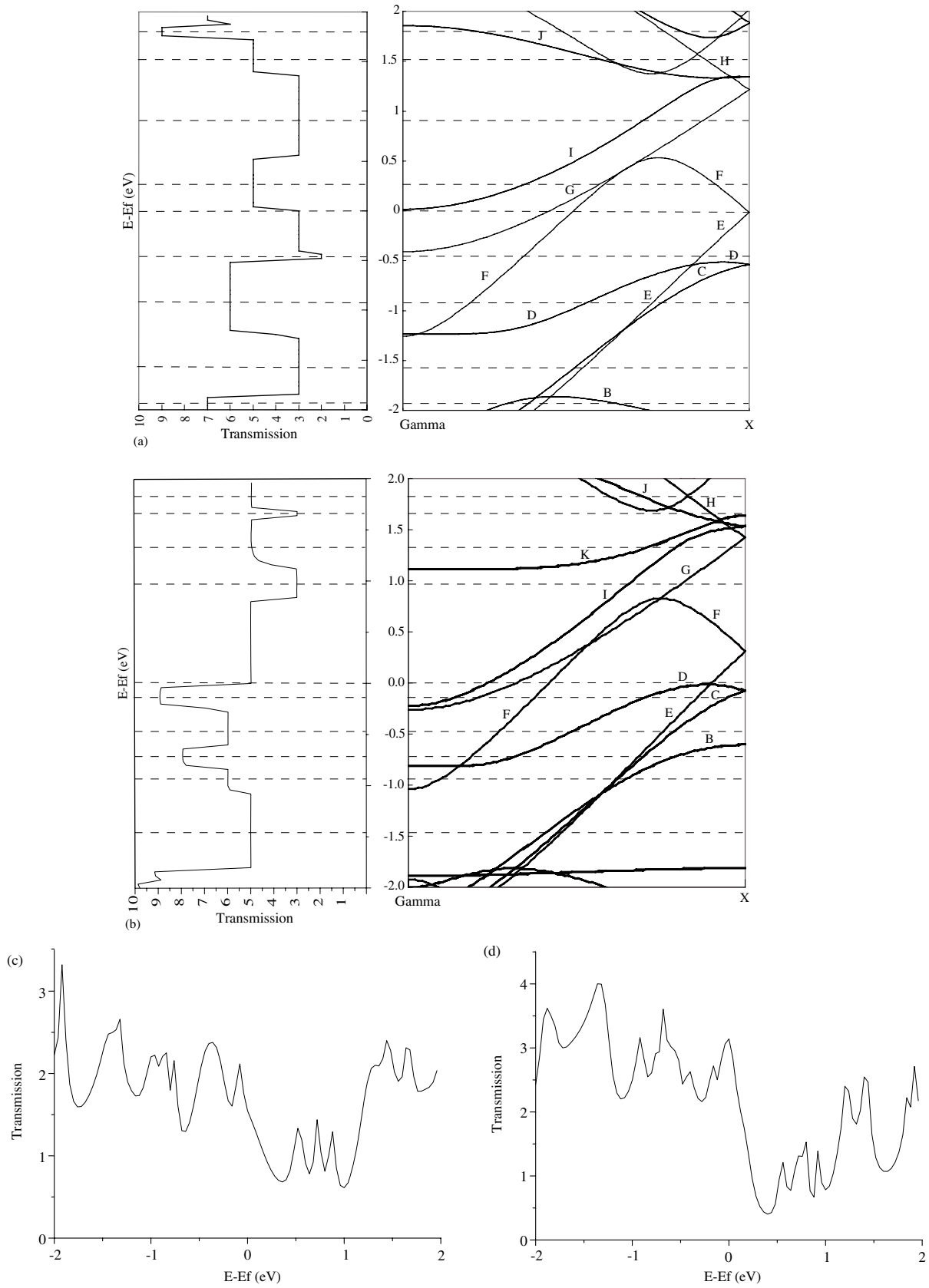


**Figure 4.** The total transmission spectra of (a) $R_{5,7}(3, 0)$–$R_{5,7}(3, 0)$–$R_{5,7}(3, 0)$, (b) $R_{5,7}(4, 0)$–$R_{5,7}(4, 0)$–$R_{5,7}(4, 0)$, (c) Au–$R_{5,7}(3, 0)$–Au and (d) Au–$R_{5,7}(4, 0)$–Au at zero bias. The correspondence between total transmission spectra and band structure of HNT electrodes is also shown in (a) and (b), marked out with dashed lines.

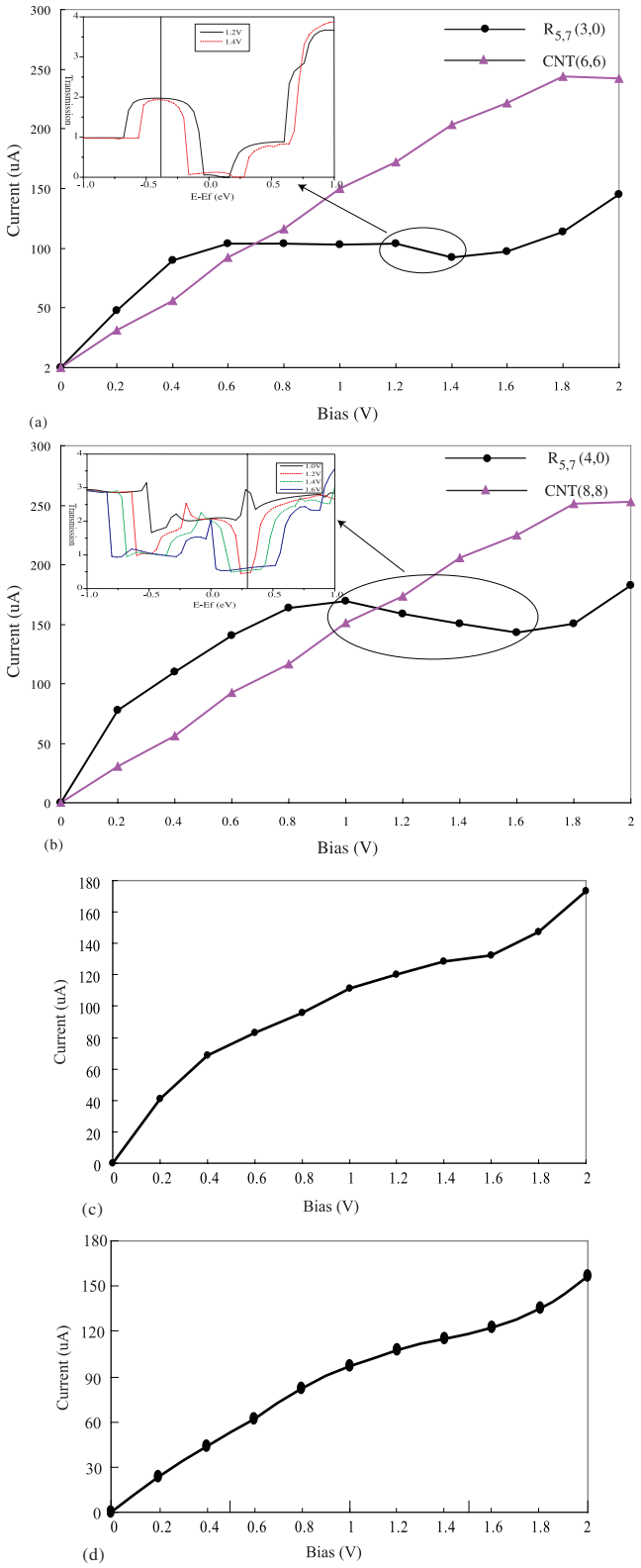


**Figure 5.** The $I$–$V$ curves of (a) $R_{5,7}(3, 0)$–$R_{5,7}(3, 0)$–$R_{5,7}(3, 0)$ (marked with a dot) and CNT(6, 6)–CNT(6, 6)–CNT(6, 6) (marked with a triangle), (b) $R_{5,7}(4, 0)$–$R_{5,7}(4, 0)$–$R_{5,7}(4, 0)$ (marked with a dot) and CNT(8, 8)–CNT(8, 8)–CNT(8, 8) (marked with a triangle), (c) Au–$R_{5,7}(3, 0)$–Au and (d) Au–$R_{5,7}(4, 0)$–Au. The bias is only applied to the left electrode, keeping the electrochemical potential of the right electrode constant. Thus, the current flow direction is from the left electrode to the right electrode (i.e. electrons flow from the right electrode to the left electrode). The insets give the total transmission spectra of HNTs in the NDR region.

length of conductance $L$ is less than the mean free path $L_m$. A ballistic conductor should have zero resistance. The resistance arising only from the interface between the device and electrodes is referred to as the contact resistance [20]. The contact resistance could be eliminated simply by making the contacts identical to the conductors. In this regime, the transmission is only given by the energy-dependent number of available conducting channels, i.e. the number of bands crossing a given energy, as shown in figures 4(a) and (b). As a comparison, transmission spectra of $R_{5,7}(3, 0)$ and $R_{5,7}(4, 0)$ coupled with bulk Au(111) electrodes are shown in figures 4(c) and (d). A wide valley with small transmission around the Fermi level is seen clearly. The equilibrium conductance of $R_{5,7}(3, 0)$ is $1.54G_0$ with five eigenchannels, while that of $R_{5,7}(4, 0)$ is $3.14G_0$ with five eigenchannels.

### *3.3. Transport properties under finite bias*

A transport calculation of two pure HNTs $R_{5,7}(3, 0)$ and $R_{5,7}(4, 0)$ has been implemented, and the $I$–$V$ curves are illustrated in figures 5(a) and (b). For comparison, the $I$–$V$ curves of their graphitic armchair counterparts CNT(6, 6) and CNT(8, 8) are also inserted. At low bias, the electrical conductivities of $R_{5,7}(3, 0)$ and $R_{5,7}(4, 0)$ are better than that of CNTs. The ratios between the conductivities of the two types of nanotube ($I_{HNT}/I_{CNT}$) are 1.6 for $R_{5,7}(3, 0)$ and 2.5 for $R_{5,7}(4, 0)$ under 0.2 V bias, which is consistent with the prediction of stronger metallicity for HNTs. At high bias, there are clearly nonlinear $I$–$V$ characteristics in the investigated voltage region, whereas CNTs tend to metallic behavior. For example, in figure 5(a), the $I$–$V$ curve of $R_{5,7}(3, 0)$ displays a platform between 0.6 and 1.2 V, and intersects with that of CNT(6, 6) at 0.7 V. The $I$–$V$ curve exhibits an NDR phenomenon in the bias range between 1.2 and 1.4 V. In figure 5(b), the $I$–$V$ curve of $R_{5,7}(4, 0)$ intersects with that of CNT(8, 8) at 1.1 V and also displays an NDR behavior between 1.0 and 1.6 V.

In order to understand the NDR behavior in the two-probe system, the transmission spectra in the NDR region for $R_{5,7}(3, 0)$ and $R_{5,7}(4, 0)$ are inserted in figures 5(a) and (b), respectively. Clearly seen in figure 5(a), the transmission peak centered at $-0.4$ eV narrows with the rise of the bias. In figure 5(b), a drastic decrease of transmission at 0.3 eV is observed. It has been reported that, in some cases, the NDR behavior originates from inhibition of the conduction channel at a certain bias [26]. To assess this effect, the molecular projected self-consistent Hamiltonian (MPSH) around the energy range in which the transmission spectrum is heavily suppressed is shown in figure 6. The MPSHs shown here are the eigenstates of the nanotube between the electrodes, which do not include the self-energies of the electrodes. It could be found that all MPSHs are spatially delocalized. Therefore, the suppressed conduction channel is not observed here. It should be noted that it is difficult to establish a correlation between the transmission peaks or valleys and the MPSH due to the fact that, in such a system, the MPSHs are broadened drastically and it is difficult to determine which one contributes to a given transmission peak or valley.

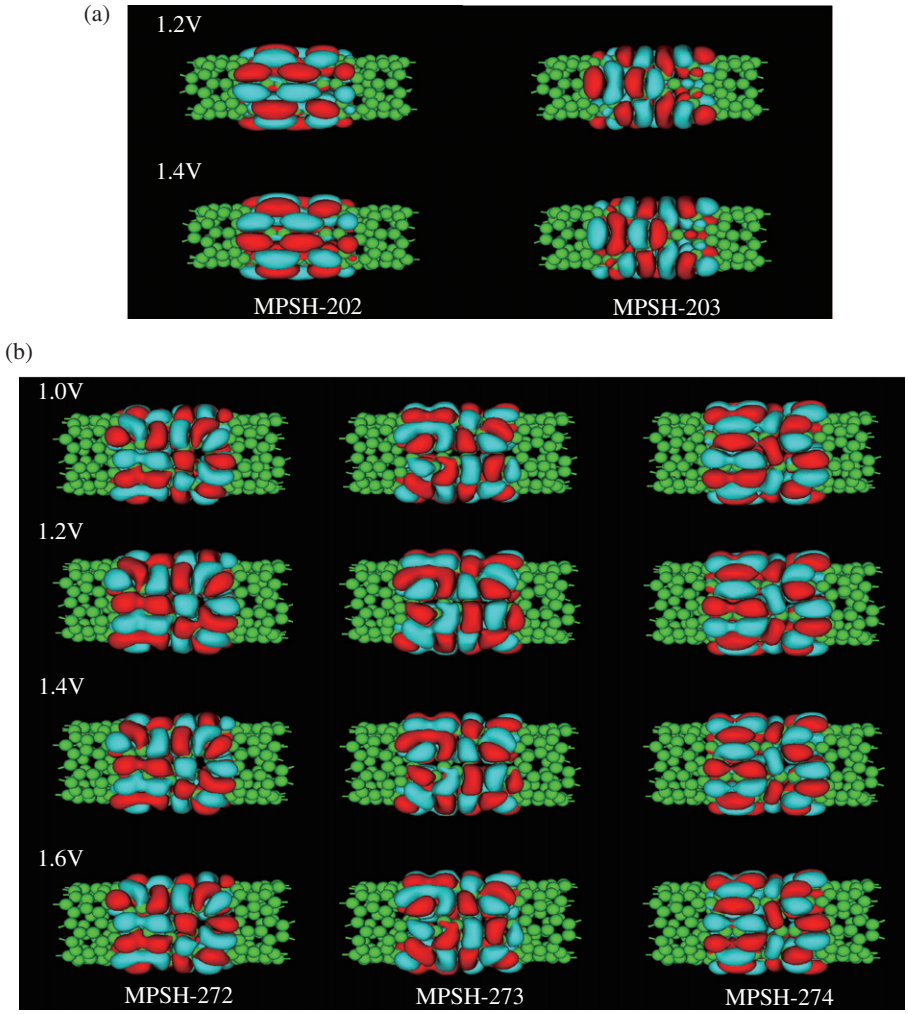


**Figure 6.** The MPSH around the area of transmission suppression of (a) $R_{5,7}(3, 0)$–$R_{5,7}(3, 0)$–$R_{5,7}(3, 0)$ and (b) $R_{5,7}(4, 0)$–$R_{5,7}(4, 0)$–$R_{5,7}(4, 0)$. The eigenvalues of MPSH-202, MPSH-203, MPSH-272, MPSH-273 and MPSH-274 are −0.36 eV, −0.35 eV, 0.35 eV, 0.36 eV and 0.42 eV, respectively.

To gain more insight into the transport properties of the HNTs, the total transmission is decomposed into individual eigenchannel contributions in the energy range of −1 to 1 eV. Figures 7 and 8 present the band match between the left and right HNT electrodes for $R_{5,7}(3, 0)$ and $R_{5,7}(4, 0)$, respectively. The eigenchannel or band marked with hollow squares is doubly degenerate. It can be seen clearly that these changes of eigenchannel transmission are consistent with the changes of band match between the two electrodes; namely, each peak in the eigenchannel transmission spectra corresponds to a band match of two electrodes. This reflects that the variation of transmission is closely related to the shift of band structures of the electrodes. For example, in figure 7(a), there exist three eigenchannels with contributions to the total transmission. Eigenchannel T1 can be divided into three parts. In the first one, from −1 to −0.04 eV, the transmission is saturated to unity, which corresponds to the overlapping by bands E and F of the left electrode and band E of the right electrode. In the second one, the transmission through eigenchannel T1 is close to zero in a small energy region from −0.04 to 0.20 eV. In the last one, eigenchannel T1 opens at 0.20 eV and the transmission quickly increases to 0.9. This corresponds to the match by bands G and H in the left electrode and band G in the right electrode. Eigenchannel T2, which arises from the overlapping by band F in the left and right electrodes, opens at around −0.7 eV but closes at −0.04 eV, saturating to unity rapidly. The doubly degenerate eigenchannel T3 is composed by two sections. Section I, which arises from the overlapping by band I in the left electrode and band D in the right electrode, appears in the energy area from −0.6 to 0.1 eV. Section II, which is attributed to the overlapping by doubly degenerate bands I and J in the left electrode and band I in the right electrode, opens at 0.6 eV and rapidly saturates to unity. The transmission of eigenchannel T3 in section I is much smaller than that of section II, which indicates that the eigenchannel contributed by dissimilar bands is less transparent than that by identical bands. When the bias increases from 1.2 to 1.4 V, the bands in left and right electrodes shift away from each other, which leads to the mismatch of bands and then the shrinkage of transmission through the eigenchannels. The reduction of transmission through eigenchannel T1 is canceled by the broadening of the

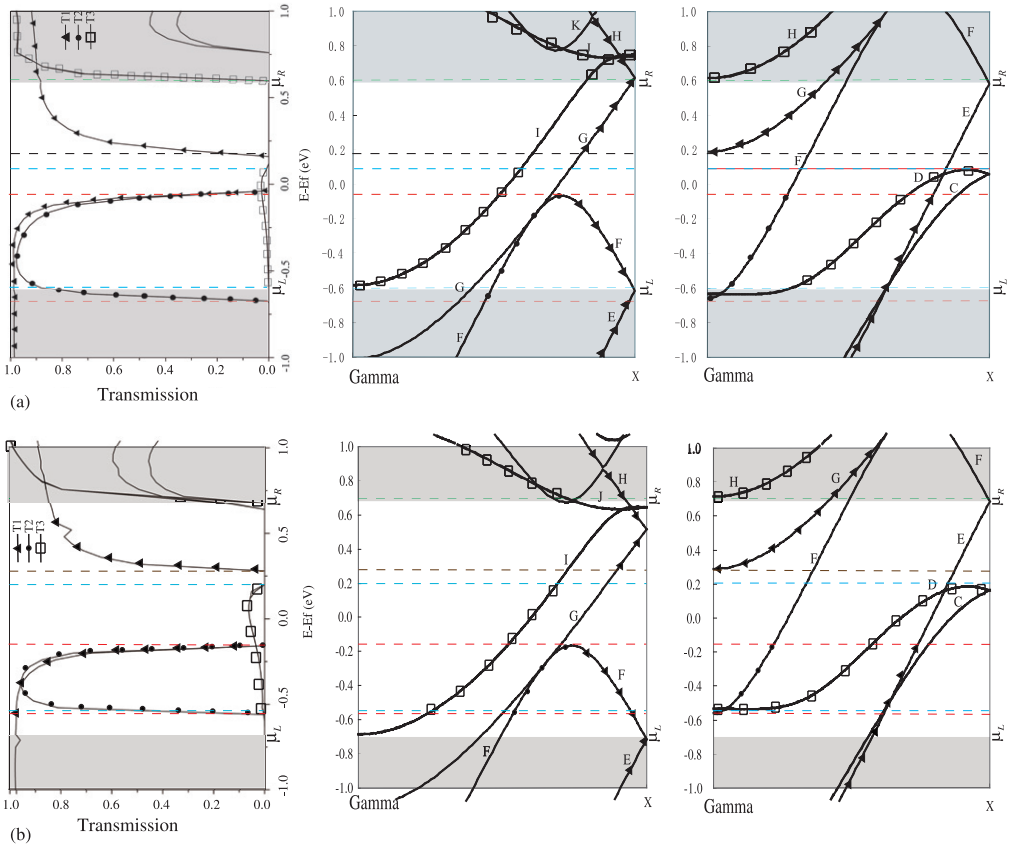


**Figure 7.** The eigenchannel decompositions and homologous band structure under bias of (a) 1.2 V and (b) 1.4 V in the NDR region of $R_{5,7}(3, 0)$–$R_{5,7}(3, 0)$–$R_{5,7}(3, 0)$. The correspondence between them is marked with dashed lines. The region not covered by gray plates is the so called current window, which contributes to the current.

current window, while the transmission through eigenchannel T2 decreases monotonically. In consequence, the application of a potential drop causes the shrinkage of the eigenchannels and thus it eventually induces the NDR behavior. With the further increment of bias, the bands in the electrodes will shift away more and more, which leads to the vanishing of eigenchannel T2, the broadening of the gap in eigenchannel T1 and the enhancement of eigenchannel T3 in section I. Figure 9(a), which illustrates the total transmission under each bias, exhibits these trends clearly.

With the same analysis, the correspondence between bias-dependent transmission spectra and band structure in $R_{5,7}(4, 0)$ is shown in figure 8. There are four eigenchannels contributing to the total transmission. Eigenchannel T1 is attributed to the overlapping by bands E and F in the left electrode and band E in the right electrode. Eigenchannel T2 is attributed to band F in the left and right electrodes. Eigenchannel T4 is attributed to the bands G and H in the left electrode and band G in the right electrode. The components of eigenchannel T3, which could be divided into four sections, are quite complex. Section I corresponds to the overlapping by bands C and D in the left electrode and band C in the right electrode. Section II corresponds to band I in the left electrode and band E in the right electrode. Section III corresponds to band I in the left electrode and band D in the right electrode. Section IV corresponds to band I in the left and right electrodes. The transmission in sections I and IV approaches unity, while that in sections II and III forms a valley giving much smaller transmission. This confirms the standpoint that the eigenchannel transmission contributed by the same band in the electrodes is larger than that by different bands. With increment of the bias, the bands in the electrodes shift away from each other, which leads to the decrease of eigenchannel T2, the more extended valley of eigenchannel T3 and a wider transmission gap between eigenchannels T1 and T4. All of these effects eventually cause the total transmission behavior and the NDR phenomenon, as shown in figure 5(b). The total transmission under each bias is shown in figure 9(b).

It is worthwhile to compare the above results with that of the same HNTs coupled with bulk Au(111) electrodes. Figures 5(c) and (d) display the $I$–$V$ curves of Au–$R_{5,7}(3, 0)$–Au and Au–$R_{5,7}(4, 0)$–Au, respectively. No NDR phenomenon appears in these systems. Here, this situation can be explained by considering two aspects arising from the band structure in electrodes and the contacts: (i) how many states are able to couple with device states and (ii) how well they are coupled. Figure 10 illustrates the band structure of the bulk Au electrode. It is shown that bulk Au has a uniform and continuous band structure in a very wide energy range, while the bands in the HNT are discrete and relatively straight.

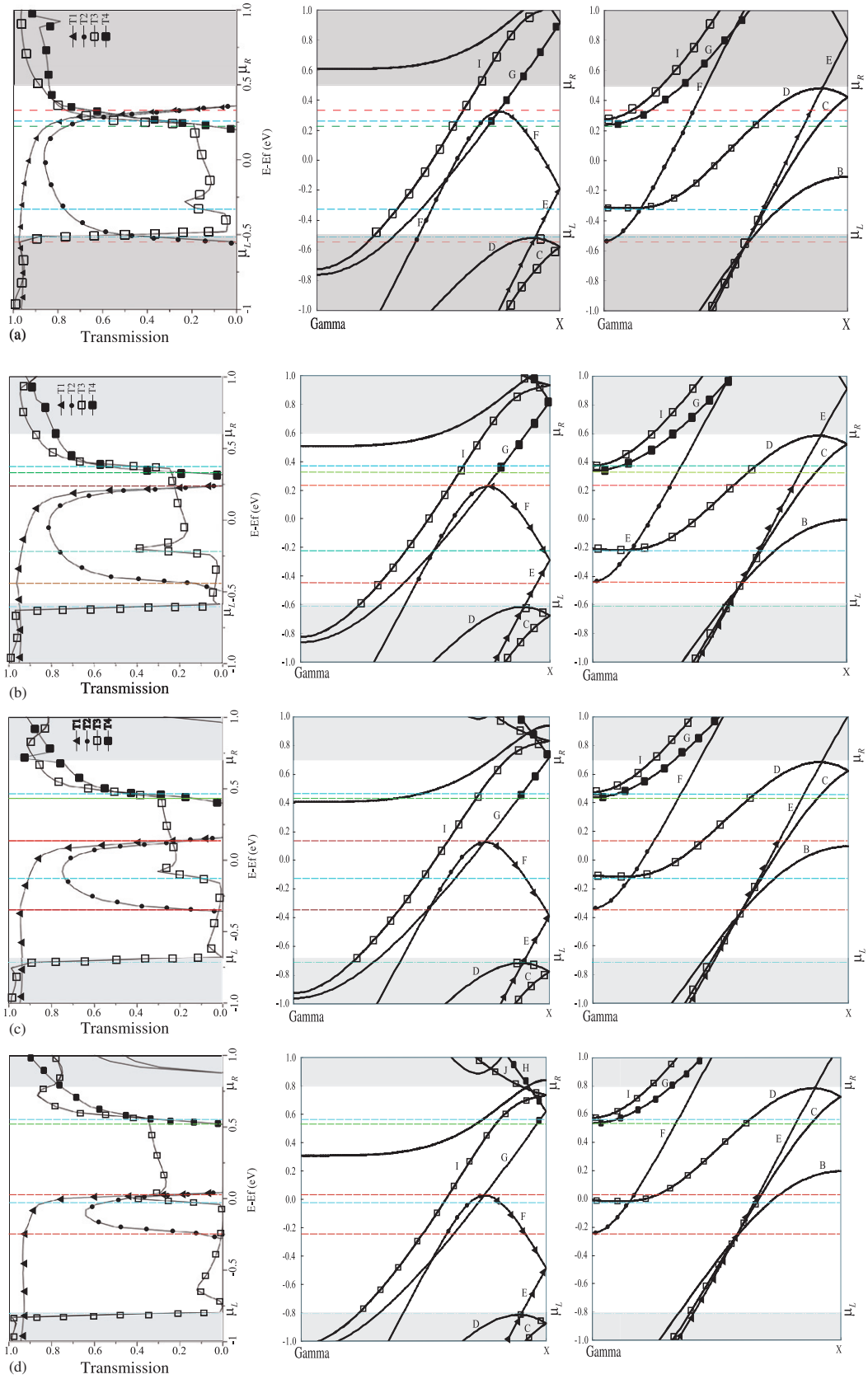


**Figure 8.** The eigenchannel decompositions and homologous band structure under bias of (a) 1.0 V, (b) 1.2 V, (c) 1.4 V and (d) 1.6 V in the NDR region of $R_{5,7}(4, 0)$–$R_{5,7}(4, 0)$–$R_{5,7}(4, 0)$. The correspondence between them is marked with dashed lines.

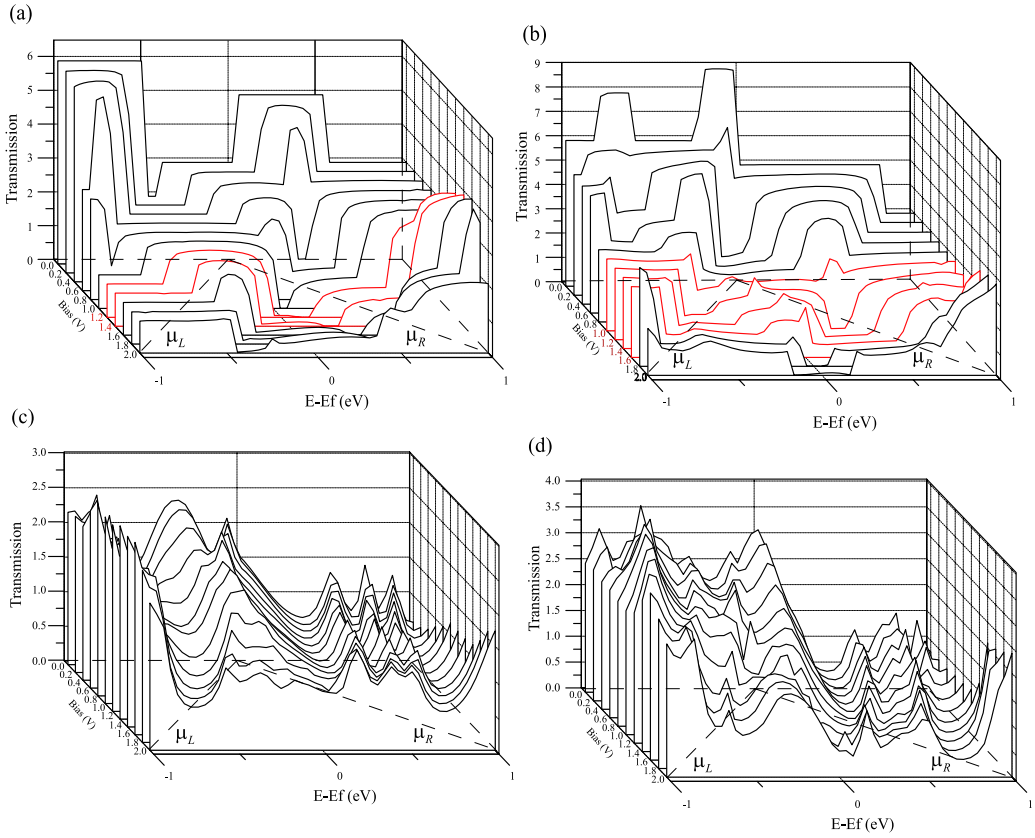


**Figure 9.** The bias-dependent total transmission of (a) $R_{5,7}(3, 0)$–$R_{5,7}(3, 0)$–$R_{5,7}(3, 0)$, (b) $R_{5,7}(4, 0)$–$R_{5,7}(4, 0)$–$R_{5,7}(4, 0)$, (c) Au–$R_{5,7}(3, 0)$–Au and (d) Au–$R_{5,7}(4, 0)$–Au under each bias.

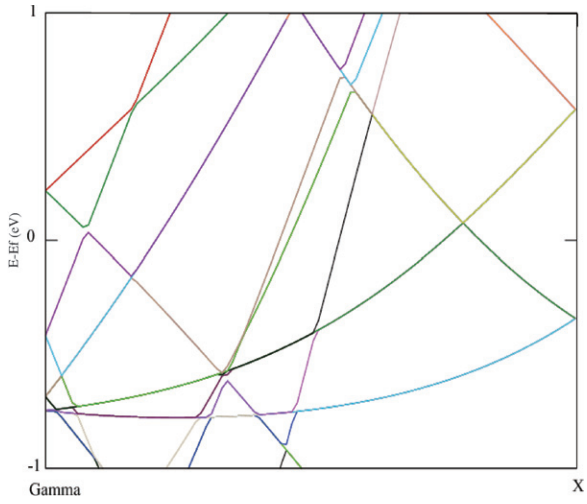


**Figure 10.** Band structure of bulk Au electrode.

Therefore, the mismatch of bands in the Au electrodes could be ignored in the investigated bias range of this paper, and the features of the transport are mainly determined by the contacts and the device itself. However, the band match between HNTs is much weaker than bulk Au for its constrictive energy bands. Figures 9(c) and (d) show the total transmission spectra of Au–$R_{5,7}(3, 0)$–Au and Au–$R_{5,7}(4, 0)$–Au under various biases. It is interesting that the transmission peaks in Au–$R_{5,7}(3, 0)$–Au and Au–$R_{5,7}(4, 0)$–Au are comparatively rigid, whereas the transmission peaks in $R_{5,7}(3, 0)$–$R_{5,7}(3, 0)$–$R_{5,7}(3, 0)$ and $R_{5,7}(4, 0)$–$R_{5,7}(4, 0)$–$R_{5,7}(4, 0)$ are very sensitive to the bias. This difference between HNT and bulk Au electrodes results in different behaviors in device performance and drastically affects their $I$–$V$ characteristics.

## 4. Conclusion

In summary, using first-principles quantum calculations, the transport properties of HNTs sandwiched between bulk Au(111) and HNT electrodes have been investigated in detail. Disquisitions in the past mainly focused on the transport effects of the central device and its contacts. However, our results show that the band topology of the lead could be determinant when the sizes of lead become similar to the central region. On further generalization of this viewpoint, if using nanoscale electrodes (such as nanowires, nanotubes and so on) instead of conventional bulk metallic electrodes, many intriguing features of $I$–$V$ characteristics such as NDR, rectification, nonlinear conduction etc may be obtained even with a simple structure. All of these questions intensely deserve further investigation.

## Acknowledgments

The authors acknowledge the financial support from the National Natural Science Foundation of China (NSFC 20503011, 20621091).

## References


[1] Kroto H W *et al* 1985 *Nature* **318** 162
[2] Kratschmer W *et al* 1990 *Nature* **347** 354
[3] Iijima S 1991 *Nature* **354** 56
[4] Crespi V H, Cohen M L and Rubio A 1997 *Phys. Rev. Lett.* **79** 2093
[5] Terrones H, Terrones M, Hernández E, Grobert N, Charlier J-C and Ajayan P M 2000 *Phys. Rev. Lett.* **84** 1716
[6] Charlier J-C 2002 *Acc. Chem. Res.* **35** 1063
[7] Milosevic I, Popovic Z, Volonakis G, Logothetidis S and Damnjanovic M 2007 *Phys. Rev.* B **76** 115406
[8] Lambin Ph, Mark G I and Biro L P 2003 *Phys. Rev.* B **67** 205413
[9] Lisenkov S, Andriotis A N, Ponomareva I and Menon M 2005 *Phys. Rev.* B **72** 113401
[10] Chen J, Reed M A, Rawlett A M and Tour J M 1999 *Science* **286** 1550
[11] Taylor J, Brandbyge M and Stokbro K 2003 *Phys. Rev.* B **68** 121101
[12] DiVentra M, Kim S-G, Pantelides S T and Lang N D 2001 *Phys. Rev. Lett.* **86** 288
[13] Pop E, Mann D, Cao J, Wang Q, Goodson K and Dai H 2005 *Phys. Rev. Lett.* **95** 155505
[14] Zazunov A, Feinberg D and Martin T 2006 *Phys. Rev.* B **73** 115405
[15] *ATK version 2.0, Atomistix A/S* www.atomistix.com
[16] Brandbyge M, Mozos J-L, Ordejón P, Taylor J and Stokbro K 2002 *Phys. Rev.* B **65** 165401
[17] Soler J M, Artacho E, Gale J D, García A, Junquera J, Ordejón P and Sánchez-Portal D 2002 *J. Phys.: Condens. Matter* **14** 2745
[18] Taylor J, Guo H and Wang J 2001 *Phys. Rev.* B **63** 245407
[19] Haug H and Jauho A-P 1996 *Quantum Kinetics in Transport and Optics of Semiconductors* (Berlin: Springer)
[20] Datta S 1995 *Electronic Transport in Mesoscopic Systems* ed H Ahmed, M Pepper and A Broers (Cambridge: Cambridge University Press)
[21] Brandbyge M, Kobayashi N and Tsukada M 1999 *Phys. Rev.* B **60** 17064
[22] Cuevas J C, Yeyati A L and Martín-Rodero A 1998 *Phys. Rev. Lett.* **80** 1066
[23] Brandbyge M, Sorensen M R and Jacobsen K W 1997 *Phys. Rev.* B **56** 14956
[24] Perdew J P and Zunger A 1981 *Phys. Rev.* B **23** 5048
[25] Huang K and Han R Q 1988 *Solid State Physics* (Beijing: High Education Press)
[26] Li X F, Chen K Q, Wang L L, Long M Q and Zou B S 2007 *Appl. Phys. Lett.* **91** 133511